Polymer 53 (2012) 2109–2120

Contents lists available at SciVerse ScienceDirect

Polymer

journal homepage: www.elsevier.com/locate/polymer

Synthetic process engineered polyaniline nanostructures with tunable morphology and physical properties

Xi Zhang [a,b], Jiahua Zhu [a], Neel Haldolaarachchige [c], Jongeun Ryu [d], David P. Young [c], Suying Wei [b,**], Zhanhu Guo [a,*]

[a] Integrated Composites Laboratory (ICL), Dan F Smith Department of Chemical Engineering, Lamar University, Beaumont, TX 77710, USA
[b] Department of Chemistry and Biochemistry, Lamar University, Beaumont, TX 77710, USA
[c] Department of Physics and Astronomy, Louisiana State University, Baton Rouge, LA 70803, USA
[d] Department of Mechanical & Aerospace Engineering, University of California Los Angeles, Los Angeles, CA 90095, USA

ARTICLE INFO

Article history:
Received 11 January 2012
Received in revised form
20 February 2012
Accepted 24 February 2012
Available online 1 March 2012

Keywords:
Polyaniline nanostructures
Magnetoresistance
Dielectrical properties

ABSTRACT

Polyaniline (PANI) nanofibers (NFs) obtained by the interfacial polymerization method are studied and compared with PANI nanostructures prepared by the ultrasonication method and the polymer acid doping method. In the case of PANI NFs, the effects of the reaction time, the size of the interfacial area, scale ratio, and concentration of reactant on the crystalline structure, thermal stability, morphology, electrical conductivity and dielectric permittivity are systematically studied. Meanwhile, huge difference in morphology is observed and related to the nanofiber growth condition. Unusual morphology and peaks on X-ray diffraction curve of PANI doped with polymer acid (poly(2-acrylamido-2-methyl-1-propanesulfonic acid)) (PAMPSA) are observed and associated with high molecular weight of the doped polymer acid. The change of the conductivity is attributed to a combination of crystallinity and crystal size. Temperature dependent conductivity reveals a 3-d variable range hopping (VRH) electron transport mechanism. The electrical conductivity and dielectric permittivity are investigated and mainly depend on the morphology and crystalline structure. The resistivity of the PANI NFs is observed to be the lowest one compared with the other two at room temperature. Both PANI nanostructures (NFs and NPs) exhibit negative real permittivity in the whole frequency range. Meanwhile, positive magnetoresistance (MR) is observed in all the three kinds of PANI nanostructures and is analyzed theoretically from the currently available wave-function shrinkage model.

1. Introduction

Conjugated polymers have attracted more attention due to their wide potential applications [1–5] arising from their unique electrochemical, optical and mechanical properties [6–11]. And among all the conjugated polymers, polyaniline (PANI) is more attractive owing to its controllable doping levels [12–14] and potential wide applications such as anticorrosion coating [15], sensors [16], reduction of toxic in water [17] and tissue engineering [18]. However, for PANI synthesized in the classical way using aniline, oxidant, and small molecule acid [19], the solubility in the common solvents is very low, which limits its applications. Even worse, the thermal degradation temperature is lower than its melting temperature [20], which excludes the traditional melting to process these conjugated polymers as used for the normal thermoplastics.

Researchers have made many efforts to solve the solubility challenge. An improved solubility can be achieved by reducing the PANI grain size [21], introducing the side groups to the PANI chains [22–24], and synthesizing PANI composites [25,26]. Though introducing the sulfonic side group to the PANI main chain from the acids such as fuming sulfuric acid [22] and 1,3-propanesultone [23] can improve the dispersibility of PANI, PANI can hydrolyze during the sulfonation reaction [13,27] and results in a decreased electrical conductivity (σ). Polymer acids such as polystyrene sulfonic acid (PSSA) [28] and poly(2-acrylamido-2-methyl-1-propanesulfonic acid) (PAMPSA) [13] as dopants to form a hybrid with PANI are found to be more suitable to enhance the dispersibility of PANI due to the residue acid groups, which did not participate in the doping process [13]. For example, PAMPSA used to dope PANI is found to improve the dispersibility with excess pendent sulfonic acid groups

* Corresponding author. Tel.: +1 409 880 7654.
** Corresponding author. Tel.: +1 409 880 7976.
E-mail addresses: suying.wei@lamar.edu (S. Wei), zhanhu.guo@lamar.edu (Z. Guo).

0032-3861/$ – see front matter © 2012 Elsevier Ltd. All rights reserved.
doi:10.1016/j.polymer.2012.02.042

in the polymer acid backbone [29]. Another way to improve the solubility of PANI is to decrease the grain size. PANI nanostructures, including nanowires, nanorods, nanotubes and nanofibers (NFs), have many advantages such as large interfacial area between PANI and their surrounding [30], which improves the dispersibility in the hosting matrices. PANI NFs have found wide applications such as multifunctional structural nanocomposites [31–33]. For example, PANI NFs with high σ and environmental stability have served as nanofillers for synthesizing epoxy [34] and poly(methyl methacrylate) (PMMA) nanocomposites with improved dielectric properties [35]. The dedoped PANI NFs are found to enhance the ionic interfacial stability of the electrolyte system [36]. PANI NFs with large specific surface area can absorb and react with chloroaurate anions ($AuCl_4^-$) to form PANI-Au nanocomposites for H_2O_2 sensing [33]. And PANI NFs can be well dispersed in collagen (naturally occurring fibrous proteins) with an enhanced σ [37].

Nanostructured PANI can be synthesized by a simple template method [37–40]. For example, silica [41] and porous poly(styrene-*block*-2-vinylpyridine) (PS-b-PVP) diblock copolymers [42] have been reported to serve as templates to prepare PANI NFs. Although, this template method can synthesize high quality PANI NFs, the yield is very low and cannot meet the large-quantity demand for industrial utilization. Electrospinning is another approach to obtain PANI NFs. The isolated PANI NFs doped with camphorsulfonic acid (CSA) electrospun with polyethylene oxide (PEO) have been used to sense the aliphatic alcohol vapors with higher sensitivity than the nanofiber mats prepared via traditional chemical synthesis [43]. However, PANI NFs obtained by electrospinning are always blended with other more soluble polymers such as PEO and PMMA, which are used to overcome the low solubility and to improve the processability of PANI [44–47]. Ways to synthesize nanostructural PANI without depending on templates or other soluble polymers are demanding. Recently, Huang and Kaner [48] reported an interfacial polymerization method, from which large amount of PANI NFs can be obtained at the interface of the two phases. The solvents for the organic phase can be benzene, hexane, toluene, carbon tetrachloride, chloroform, methylene chloride, diethyl ether, carbon disulfide [49], or *o*-dichlorobenzene [48]. The shape and size of PANI are reported to be independent of the solvent [48]. Similarly, various dopants can be used to accomplish the interfacial polymerization, including phosphoric acid, acetic acid, formic acid, tartaric acid, methylsulfonic acid, ethylsulfonic acid, CSA [49] and 4-toluene sulfonic acid [48]. PANI NFs with different fiber thickness can be synthesized with different dopants. Interfacial polymerization synthesized NFs appear to be insensitive to the polymerization temperature and monomer concentration, but are affected by the acid concentration. Magnetic stirring during the interfacial reaction caused the agglomeration of NFs at the surface of the emulsion droplets [48]. However, the relationship between the morphology (length, size and aspect ratio) of the NFs and the used interfacial surface area (given the same amount of materials) has not been reported. Furthermore, the property comparison among the different morphologies synthesized from different methods has been rarely reported, though it is demanding for academic interests and engineering applications.

Giant magnetoresistance (GMR), defined as a large change in resistance when the relative orientation of the magnetic domains in adjacent layers is adjusted from anti-parallel to parallel under an applied magnetic field, is first discovered in alternating ferromagnetic iron and non-ferromagnetic chromium layers [50]. Recently, GMR phenomenon reported in the organic systems, a potential alternative to metals in GMR sensors, has attracted much attention due to its unique properties including semiconductive, light weight and little spin-orbit coupling [51]. To the best of our knowledge, most of the current research on the MR behaviors in organic semiconductors is still in a state of modeling and theoretical prediction [51]. In different models, various polarons are included, such as in electron-hole (*e*-*h*) pair models [52], the anomalous MR in the semiconductor is related to the recombination limitation of the electrons and holes. And the bipolaron model [53] with the effects of the electron and hole being studied separately can be used to explain the transition between positive and negative MR. And the organic magnetoresistance (OMR) is generally believed to originate from spin correlations among the interacting charge carriers. And a good understanding of the mechanism of MR will be beneficial to the applications of the semiconductors [54]. In addition, due to the tunable electronic property and easy processability, π-conjugated organic semiconductors have significant technological applications such as information display and large-area electronics [55]. And owing to the unique negative physical properties such as refractive index and permittivity, metamaterials have attracted great interests. Recently, negative permittivity is discovered by our group in the conductive polymer-based nanocomposites (PNCs) such as polyaniline–tungsten oxide and polypyrrole–tungsten oxide [8,9] and carbon nanofibers (CNFs)/elastomer PNCs [56]. These materials obtain a promising future that can be applied in cloaking, superlens, wave filters, remote aerospace applications, and superconductors [57–59]. However, the MR and negative permittivity, especially with a combined MR and negative properties in a semiconductive PANI nanostructure, has been rarely reported.

In this paper, the interfacial polymerization process for synthesizing PANI nanofibers (NFs) has been systematically investigated from an engineering aspect and the synthesized NFs are compared with the ones obtained from the other two synthesis methods, i.e., ultrasonication and polymer acid doping. In the case of interfacial polymerization method, the morphology of PANI NFs is studied by varying the parameters including the interfacial area between two phases with a fixed amount of reactants and solvents, polymerization time, concentration, and scale-down by varying the amount of reactants and solvent while maintaining the same interfacial area. The morphology, crystallinity, electrical conductivity (σ), dielectric permittivity, and thermal stability of the obtained different PANI nanostructures are investigated and compared. The electron conduction mechanisms are explored by studying the temperature dependent conductivity. The magnetic field dependent resistance (MR) is measured in the obtained nanostructures and is interpreted from the currently available wave-function shrinkage theory.

2. Experimental

2.1. Materials

Aniline (C_6H_7N), ammonium persulfate (APS, $(NH_4)_2S_2O_8$), *p*-toluene sulfonic acid (PTSA, $C_7H_8O_3S$) and poly(2-acrylamido-2-methyl-1-propanesulfonic acid) (PAMPSA, $M_w = 2{,}000{,}000$ g/mol) solution are all purchased from Sigma Aldrich. Chloroform ($CHCl_3$) is purchased from Fisher Scientific. All the chemicals are used as-received without any further treatment.

2.2. Preparation of PANI nanostructures

2.2.1. PANI nanofibers (NFs)

PANI NFs were prepared by the reported interfacial polymerization [48] and all the samples were prepared with the same ratio, aniline:APS:PTSA = 8:2:25. The reference sample (PANI-2), which was used as reference being compared with PANI nanostructures prepared under other different conditions, was prepared in a 200 mL beaker with a large interfacial area of 3115.66 mm^2. The

synthesis procedures are briefly described here. First, aniline (3.2 mmol) was dissolved in chloroform (10 mL) as solution one, and solution two is APS (0.8 mmol) dissolved in 10 mmol PTSA aqueous solution (10 mL deionized water). Then, solution two was added into solution one for polymerization at room temperature. And after 2-h reaction, the product was vacuum filtered and washed with ethanol and deionized water to remove excess acid, possible oligomers and organic solvent. The obtained powders were dried completely at 50 °C.

Three series of PANI NFs were prepared. For time series, the polymerization time was controlled as 15 min (PANI-1), 2 h (reference, PANI-2) and 9 h (PANI-3). For the scale-up sample PANI-4 vs PANI-2, all chemicals including reactant and solvent were one forth of those used for synthesizing the reference sample (PANI-2). For interfacial area series (PANI-4, PANI-5, and PANI-6), all chemicals were one forth of those as used for synthesizing the reference sample (PANI-2) and the interfacial area is varied, i.e. 3115.66 mm^2 for PANI-4, 1721.54 mm^2 for PANI-5 and 1157.53 mm^2 for PANI-6. And for concentration-up samples (PANI-7, PANI-8, and PANI-9), solvent was one forth of that used for synthesizing the reference sample while the reactants were still the same as those used for synthesizing the reference sample. In both scale-up and concentration-up series, the effect of interfacial area was also investigated by using 80-mL beakers with an interfacial area of 1721.54 mm^2 (PANI-5, PANI-8) and 40-mL beakers with an interfacial area of 1157.53 mm^2 (PANI-6, PANI-9) to perform the interfacial polymerization, and represented as middle size and small size of the interfacial area. Samples prepared under different conditions were named as PANI-1 – PANI-9 and the detailed synthetic conditions are summarized in Table 1.

2.2.2. Preparation of PANI NPs

PANI NPs have been prepared following our prior procedures [9]. The molar ratio used in this method was aniline:APS:PTSA = 6:3:5. For solution one, PTSA (60 mmol) and APS (36 mmol) were dissolved in deionized water (400 mL), then the solution is put in an ice-water bath under ultrasonication for 1 h. Solution two is aniline (72 mmol) dissolved in deionized water (100 mL). Then solution two was added into solution one and the mixture was sonicated for additional 1 h in an ice-water bath for polymerization. Finally, the product was vacuum filtered and further treated and washed with ethanol and deionized water to remove excess acid, possible oligomers and organic solvent. The obtained powders were dried completely at 50 °C.

2.2.3. Preparation of PANI-PAAMPSA

The PANI-PAAMPSA is prepared following the procedures reported by Loo et al. [14]. A molar ratio of aniline:APS:PAAMPSA = 1:0.9:1 was used. PAAMPSA (0.028 mol) and aniline (0.028 mol) were dissolved in deionized water (342 mL) and was stirred at room temperature for 1 h and then moved to an ice-water bath. APS (0.025 mol) was dissolved in another 25 mL deionized water, which was added dropwise to the former solution. The polymerization reaction was continued overnight and maintained in the ice-water bath for the first 6 h and vigorously stirred through the whole process. The final solution was dried at 50 °C overnight to obtain a thin film, which is further grinded into powders. The powders were washed by acetone and deionized water, and then vacuum filtered and again washed with ethanol and deionized water to remove excess acid, possible oligomers and organic solvent. The obtained powders were dried completely at 50 °C.

2.3. Characterization

2.3.1. Crystalline structure of PANI

The crystalline structure of PANI was studied by X-ray diffraction (XRD) analysis, which was accomplished in a Bruker D8 Focus diffractometer equipped with a Sol-X detector using a copper radiation source. Data were collected in the range of $2\theta = 5–35°$ at a resolution of 0.05° per step with a 6-s integration time per step. The crystallinity of the PANI nanostructures is calculated by TOPAS software and is obtained as the crystalline area divided by the sum of crystalline area and amorphous area [60].

2.3.2. Morphological characterizations of PANI

The morphology of the PANI nanostructures was characterized with a scanning electron microscope (SEM, JEOL field emission scanning electron microscope, JSM-6700F).

2.3.3. Thermal characterization of PANI

Thermal degradation property of the PANI was studied by a thermogravimetric analysis (TGA, TA instruments Q-500). All PANI samples were heated from 30 to 700 °C with an air flow rate of 60 mL/min and a heating rate of 10 °C/min. Differential scanning calorimeter (DSC, TA Instruments Q2000) measurements were implemented under a nitrogen flow rate of approximately 20 mL/min at a heating rate of 10 °C/min from 30 to 400 °C.

2.3.4. Electrical conductivity and resistivity measurement

The electrical conductivity (σ) was measured by a four-probe technique in a Keithley 2400 SourceMeter under voltage-source testing mode. The measured voltage was adjusted in the range of −10 to 10 V. The corresponding current was measured and recorded across the two outer probes. The dielectric permittivity was measured by an LCR meter (Agilent, E 4980A) equipped with a dielectric test fixture (Agilent, 16451B) at the frequency of 20–2M Hz. A piece of rectangular standard Teflon sample with a permittivity of 2.1–2.4 is used for calibration before the test.

Table 1
Synthetic conditions, lattice plane spacing and the average crystallite size of (110) lattice plane of different PANI nanofiber samples.

Sample name	Reaction time	Interfacial area	Scale ratio	Concentration ratio	Crystallinity (%)	hkl (110)	
						d (Å)	L (Å)
PNAI-1	15 min	L	1	1	8.31	3.54	33.24
PANI-2	2 h	L	1	1	9.42	3.54	29.61
PANI-3	9 h	L	1	1	11.91	3.54	30.73
PANI-4	2 h	L	1/4	1	11.80	3.52	29.62
PANI-5	2 h	M	1/4	1	12.06	3.52	38.79
PANI-6	2 h	S	1/4	1	11.70	3.54	41.76
PANI-7	2 h	L	1	4	15.76	3.50	35.42
PANI-8	2 h	M	1	4	14.44	3.49	49.36
PANI-9	2 h	S	1	4	17.78	3.49	40.75

Note: Scale ratio refers to the total reactant volume with the same concentration; and concentration ratio refers to the used reactant concentration doubled while maintained the volume the same. Both are based on PANI-2 (reference sample). Large size interfacial area is 3115.66 mm^2, middle size interfacial area is 1721.54 mm^2 and small size interfacial area is 1157.53 mm^2, respectively.

The PANI NPs were pressed in the form of disc pellets with a diameter of 25 mm by applying a pressure of 95 MPa in a hydraulic presser and the average thickness was about 0.5 mm. The same sample was used to measure the electrical resistivity by a standard four-probe method in the temperature range of 50–290 K. The temperature dependent resistivity was used to investigate the electron transport mechanism in the PANI nanostructural samples. The magnetic field dependent resistance is carried out using a standard four-probe technique.

3. Results and discussion

3.1. X-ray diffraction

Fig. 1 shows the XRD patterns of the PANI NFs, synthesized from different conditions. All the nanofiber samples mainly have three peaks with 2θ at 15, 20 and 25.25°, which correspond to the (010), (100), and (110) plane of PANI, respectively [61]. The synthetic conditions are observed to have a significant impact on the crystalline structures. Only concentration-up samples (PANI-7, PANI-8 and PANI-9) have obvious peak at 2θ of 15°. In addition, the peaks of (100) and (110) in the concentration-up samples (PANI-7, PANI-8 and PANI-9) are much sharper and narrower than those of the reference sample (PANI-2). The XRD patterns of the crystalline structures can be used to estimate the average crystallite size, lattice plane d-spacing and crystallinity. The average crystallite size of the PANI NFs is estimated from the XRD patterns using Scherrer formula [62], Equation (1):

$$L = \frac{k\lambda}{\beta \cos\ \theta} \tag{1}$$

where, L is the average crystallite size, k is the shape factor and is normally 0.9, λ is the X-ray wavelength ($\lambda = 1.5406$ Å), β is the full-width at half-maximum (FWHM), FWHM was obtained from data file of XRD result, firstly the height of peak is calculated to obtain the number of half-maximum intensity, and then the two points from the XRD pattern having the half-maximum number were found, finally, FWHM is the subtraction of the 2 theta degree of the two points. And θ is the diffraction angle. And the lattice plane d-spacing is calculated based on Bragg formula [7], Equation (2):

$$\lambda = 2d\sin\ \theta \tag{2}$$

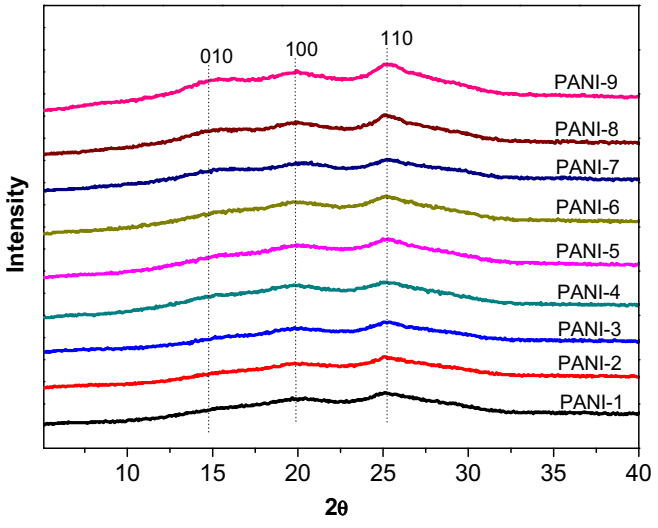

Fig. 1. X-ray diffraction patterns of the PANI nanofibers.

The d-spacing and the average crystallite size at (110) plane of PANI are summarized in Table 1. And a calculated d-spacing is observed with comparable sizes for all the PANI nanostructures synthesized from different synthetic conditions, Table 1. From the Bragg formula, d-spacing is only associated with the diffraction angle 2θ. The (110) planes of all samples are located at almost the same 2θ value without any obvious peak shift, Fig. 1. This indicates that the d-spacing does not change obviously as the synthetic conditions are changed. However, the average crystallite size (L) is observed to be significantly different in the PANI nanostructures synthesized in various conditions. From Table 1, an increased concentration causes L increased drastically (PANI-7 vs PANI-2). And in the scale-down series (PANI-4, PANI-5, PANI-6), a decreased interfacial area leads to an increased L as well. L is decided by two factors, i.e., diffraction angle and the FWHM. A narrow peak means smaller FWHM and an increased L. Compared with reference sample (PANI-2), the decreased scale (PANI-4) is observed not to change L. However, when the interfacial area (PANI-6) is decreased simultaneously, L is found to increase significantly. On the other hand, based on the crystallinity of PANI NFs summarized in Table 1, concentration-up and interfacial area decrease result in a more crystalline nanostructure with larger size.

For the interfacial polymerization, only the initial molecules located at the aqueous and organic interface can act as nucleation sites for the growth of the PANI chains [48]. In the interfacial area series (PANI-4, PANI-5, PANI-6) with a reduced amount of reactants and solvents, the available nucleation sites are reduced, which favors the formation of PANI with larger crystal size and longer polymer chains. However, in concentration-up series (PANI-7 vs PANI-2), when the concentration increases, more initial molecules are available in the interface and lead to more nucleation sites for a higher crystallinity, which is consistent with the sharp peak observed in XRD, Fig. 1. And in the concentration-up series, due to the increased number of the nucleation sites, the crystallization process is much more intensive, which causes nonuniform crystallites different from other samples and thus leads to a nonobvious trend of the average crystalline size with a simultaneously reduced interfacial area size.

Fig. 2 shows the XRD patterns of (a) PANI NFs (PANI-2), (b) PANI NPs prepared by ultrasonication, (c) PANI-PAMPSA polymer hybrid, (d) pure APS and (e) pure PAMPSA polymer acid. Though no obvious peak shift is observed in the PANI nanoparticle sample synthesized by ultrasonication (the d-spacing value is 3.5381 Å equal to PANI NFs), poorer crystallinity (7.48%) and larger average crystallite size are suggested based on the facts that the height of peaks at 2θ of 20 and 25.25° are much lower than those of PANI-2. In addition, the L value of (110) plane is 45.2522 Å, which is lager than that of PANI-2. The broad and weak peak of the PAMPSA, Fig. 2(e), indicates a poor crystalline structure of the polymer acid. In the PANI-PAMPSA sample, the observed peaks at 2θ of 19.2, 30.35, 36.15 and 40.5° are from the residue crystalline APS, Fig. 2(c,d). However, the two addition peaks at 2θ of 23.4 and 26° are observed in the PANI-PAMPSA sample. The peaks at 2θ of 23.4 and 26° might be (100) and (110) planes of PANI, respectively. As compared with the (110) plane at 25.15° of PANI synthesized by PTSA, a shift to a higher angle is noticed, which indicates a strong interaction between PANI and polymer acid. The observed shift is attributed to the subchain alignment. In the PANI-PAMPSA sample, PAMPSA chain is bonded ionically with PANI, when the PANI chains are arranged and form a crystalline structure, PAMPSA may act as side chains, which will follow the backbone's arrangement and form a layer between the lattices of PANI, thus cause a decreased d-spacing at a higher angle in the XRD pattern [12,14,63,64].

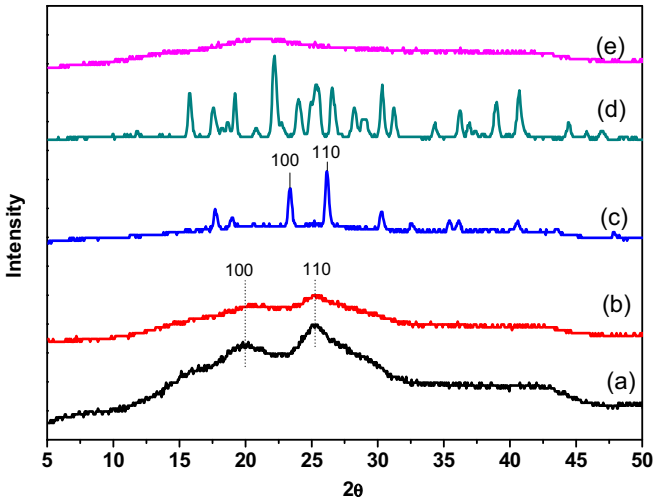

Fig. 2. X-ray diffraction patterns of (a) PANI nanofibers, (b) PANI nanoparticles, (c) PANI-PAMPSA, (d) APS, and (e) PAMPSA.

3.2. Morphology of PANI

Fig. 3 shows the SEM microstructures of the PANI NFs prepared in different conditions, and it can be observed from the SEM graph that the diameter of PANI NFs is fairly uniform. And the physical parameters (diameter, length and aspect ratio) of the NFs are summarized and shown in Table 2. For the samples prepared with different reaction time (PANI-1, PANI-2, PANI-3), the average diameter of the NFs increases with increasing the interfacial polymerization time, which is consistent with the following polymerization mechanism for the PANI nanofiber formation. The PANI NFs exist at the very beginning during the traditional polymerization process to synthesize PANI. However, with the progress of the polymerization, the formed NFs will serve as scaffolds for the further growth of PANI and finally develop to a particle form [48]. Thus, a longer polymerization time favors the formation of thicker NFs.

For the scale-down samples (PANI-4 vs PANI-2), the diameter decreased from 142.7 nm (PANI-2) to 135.3 nm (PANI-4). The NFs (PANI-4) have an average length of 1.29 μm, which is much longer than that of the reference sample (PANI-2) with an average length of 1.00 μm, which demonstrates that the decreased scale can provide a condition to synthesize larger NFs. In addition, interfacial area has an influence on the morphology of the NFs, compared with samples PANI-4, PANI-5, and PANI-6. The mean diameter of the NFs

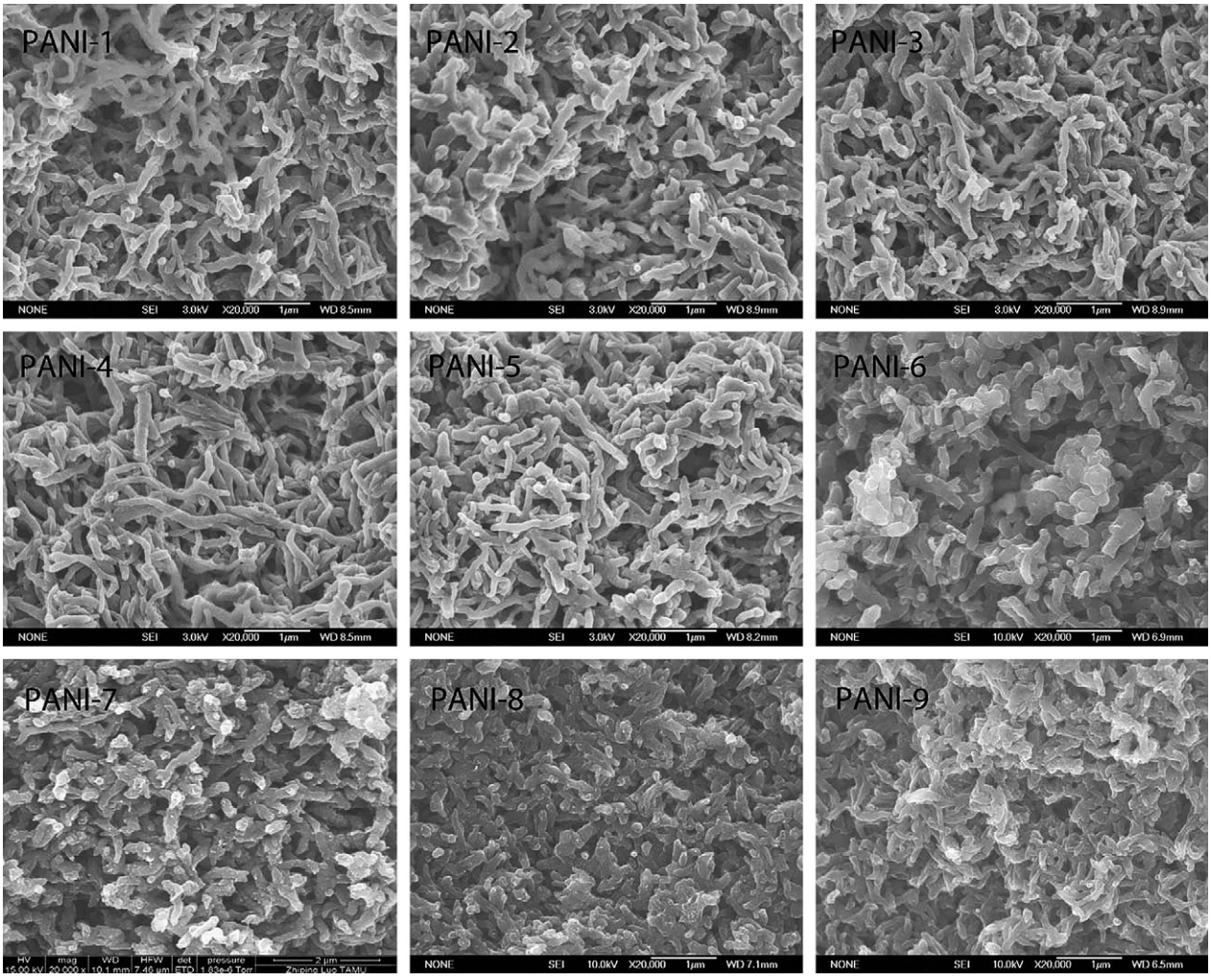

Fig. 3. SEM microstructures of the PANI nanofibers prepared in different conditions.

Table 2
Diameter, length and aspect ratio of the PANI NFs prepared in different conditions.

Samples	Diameter (nm)	Length (μm)	Aspect ratio
PANI-1	124.2	0.94	7.57
PANI-2	142.7	1.00	7.01
PANI-3	150.3	1.00	6.65
PANI-4	135.3	1.29	9.53
PANI-5	147.0	0.84	6.80
PANI-6	174.8	0.63	3.60
PANI-7	106.0	0.67	6.32
PANI-8	109.1	0.61	5.59
PANI-9	133.1	0.51	3.83

increases with decreasing the interfacial area. The same tendency is also observed in the concentration-up series (PANI-7, PANI-8 and PANI-9). For the interfacial polymerization process, the reaction takes place at the interface and thus forms the NFs there. In the case with a decreased interfacial area, less surface area is available for the growth of the NFs, which will cause NFs stick together and form thicker NFs. Meanwhile, a decreased interfacial area will limit the growth of the NFs, Fig. 3, PANI-6 with an average length of 0.63 μm and an average diameter of 174.8 nm, which are shorter and thicker than the NFs of PANI-4 with an average length of 1.29 μm and an average diameter of 135.3 nm, Table 2.

For concentration-up samples (PANI-7 vs PANI-2), the NFs not only have a smaller average diameter, but also become shorter. The average length of the NFs is 0.67 μm for PANI-7, which is much shorter than PANI-2 (1.00 μm). This special morphology is due to the intensive reaction conditions. As aforementioned in the crystalline structure analysis part, more initial molecules are available in the interface in the concentration-up samples and the system has a higher reaction rate. The formed NFs do not have adequate time to grow up and thus relatively tiny NFs are observed in the concentration-up samples.

PANI obtained under ultrasonication is also in the nanoscale level. Instead of a nanofiber structure, spherical shape is observed, Fig. 4(b). And, the small NPs tend to agglomerate and form large particles. On the other hand, the PANI doped with PAMPSA polymer acid has a completely different morphology as compared with the PANI NFs, Fig. 4(c), and PANI NPs, Fig. 4(b). The PANI-PAMSPA exhibits a flake shape and looks like a brittle plastic fracture surface, Fig. 4 (a). This special composite morphology [65] is caused by the long-chain structure of the utilized PAMPSA polymer acid, which serves as template for the growth of PANI.

3.3. Thermogravimetric analysis

Fig. 5(A) shows the TGA curves of the PANI nanostructures prepared in different conditions. All the samples have three weight loss stages. The first stage from room temperature to 150 °C is attributed to the release of the moisture and the residue organic solvent entangled in the polymer chains. The second stage between 250 and 350 °C is caused by the loss of the doping acid [66,67]. The third stage arises from the degradation of PANI. The degradation temperature increases slightly with extending the preparation time (PANI-1, PANI-2, PANI-3) and decreasing the scale (PANI-4 vs PANI-2), Table 3. However, with the increase of the reactant concentration (PANI-7 vs PANI-2), the onset decomposition temperature is increased intensely and the weight loss is decreased. The second weight loss stage almost disappears for the concentration-up samples (PANI-8 and PANI-9), Fig. 5(A). This improved thermal stability in PANI-8 and PANI-9 in the second temperature range is caused by the increased crystallinity in PANI-8 and PANI-9. In other words, the second weight loss stage is associated with the lost doping acid. It would need more energy for the acids to be removed from the polymer chains if the PANI chains doped with acid are well arranged in a more crystalline structure. Thus, the second weight loss stage of samples with higher crystallinity will shift to higher temperature and overlap with the third weight loss stage. With further increasing the temperature, the third weight loss stage ranging from 350 to 600 °C is observed with a rapid weight loss in all the samples, which is due to the breakdown of the backbone [68,69].

Table 3 also shows the degradation information of the PANI NFs, PANI NPs and PANI-PAMPSA. For PANI prepared with different methods, the thermal stability is changed significantly, Fig. 5(B). The PANI NPs are the most stable one, with a slightly weight loss in the second stage. And the PANI-PAMPSA has the poorest thermal stability. Although the onset temperature of the PANI-PAMPSA is higher than the PANI NFs and PANI NPs, it has a much larger weight loss fraction of 21.85% than the PANI NPs and PANI NFs in the second stage, which is 3.70% and 10.00% respectively. The larger weight loss in the second stage is attributed to the degradation of PAMPSA.

3.4. Differential scanning calorimetry

The DSC curves of PANI prepared with various conditions are shown in Fig. 6(A). There are two endothermic transitions ranging from 50 to 150 °C and 250–350 °C, respectively. Fig. 6(B) shows the DTG and DSC curves of PANI-1. Both transitions in the DSC curve agree with those of the DTG curve. The first one is the evaporation of moisture and residue organic solvent. The second one is an endothermic process of the loss of the doping acid instead of a glass transition [63]. Based on the prior report, the glass transition temperature (T_g) is not evident in the thermographs [9]. In addition, there is a weight loss in the temperature range between 275 and 300 °C in the DTG curve, and the glass transition, which is a phase

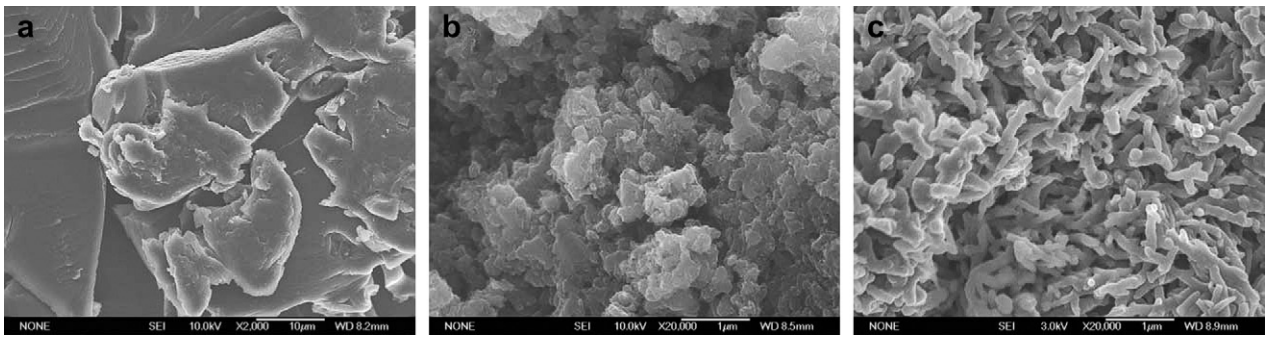

Fig. 4. SEM images of (a) PANI-PAMPSA, (b) PANI nanoparticles, and (c) PANI nanofibers.

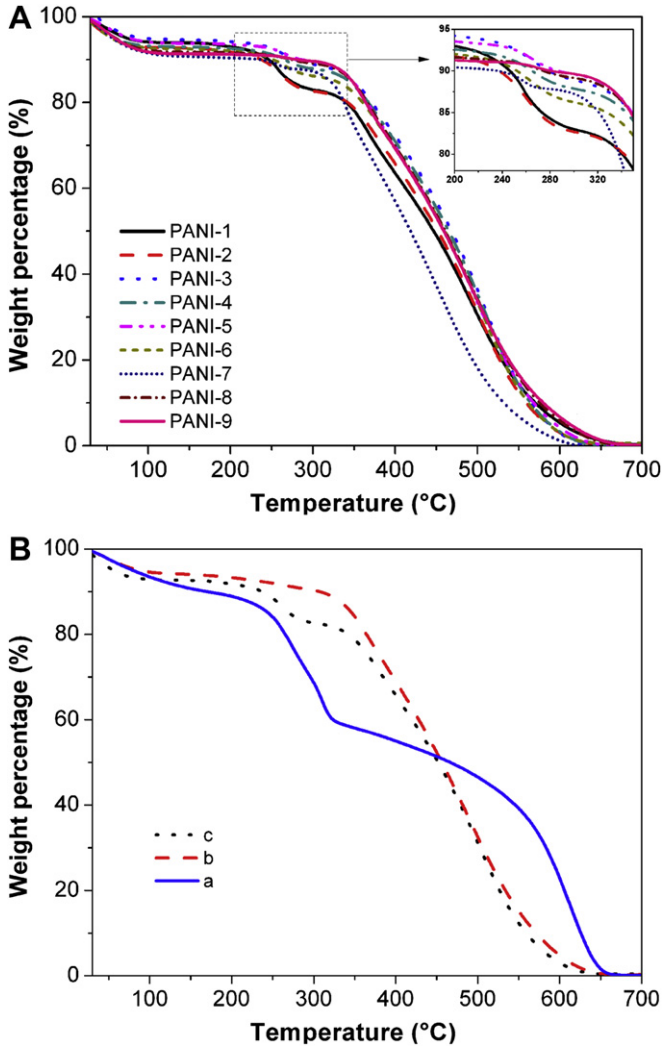

Fig. 5. (A) TGA curves for PANI nanofibers, (B) TGA curves of (a) PANI-PAMPSA, (b) PANI nanoparticles, and (c) PANI nanofibers.

change, will not cause the weight loss. The decomposition enthalpy (ΔH) and temperature values of the second endothermic process are summarized and listed in Table 4, with polymerization time increased (PANI-1, PANI-2, PANI-3), and scale down (PANI-4 vs PANI-2) the enthalpy decreased with temperature increased, which means the decomposition process will release more energy in the lower temperature range.

Table 3
Onset temperature and weight loss in 150–300 °C for PANI nanofibers prepared in different conditions, PANI nanoparticles, and PANI doped with PAMPSA.

Samples	Onset temperature (°C)	Weight loss (%) in 150–300 °C
PANI-1	233.05	10.920
PANI-2	231.62	9.968
PANI-3	233.05	5.696
PANI-4	236.32	5.041
PANI-5	240.92	4.203
PANI-6	233.30	6.246
PANI-7	242.62	3.462
PANI-8	244.20	3.005
PANI-9	248.57	1.729
PANI nanoparticle	213.56	3.699
PANI-PAAMPSA	243.92	21.85

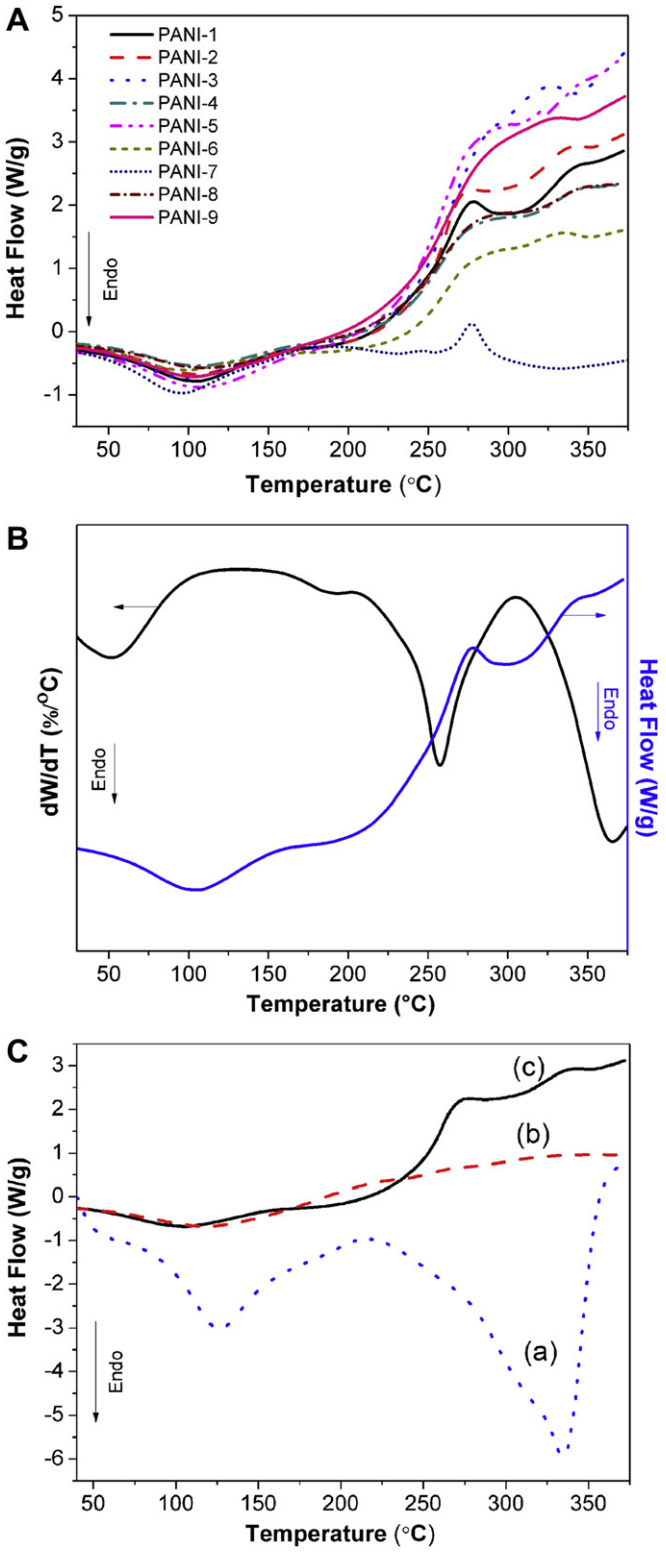

Fig. 6. (A) DSC curves of the PANI nanofibers, (B) DSC and DTG curves of PANI-1 nanofibers, and (C) DSC curves for (a) PANI-PAMPSA, (b) PANI NPs, and (c) PANI nanofibers.

Consistent with what is shown in the TGA curve, with an increased onset decomposition temperature, Fig. 5(A), the thermal stability of the scale down (PANI-4, PANI-5, PANI-6) and concentration-up (PANI-7, PANI-8, PANI-9) samples are slightly

Table 4
DSC characteristics of the second endothermic transition of PANI nanofibers prepared in different conditions, PANI nanoparticles, and PANI doped with PAMPSA.

Samples	T (°C)	ΔH (J/g)
PANI-1	280.11	94.62
PANI-2	282.64	31.56
PANI-3	330.43	30.67
PANI-4	298.82	15.41
PANI-5	318.33	30.08
PANI-6	339.43	24.23
PANI-7	278.19	104.1
PANI-8	298.15	20.10
PANI-9	331.33	19.81
PANI nanofibers (PANI-2)	282.64	31.56
PANI nanoparticles	228.91	4.438
PANI-PAAMPSA	278.67	712.6

improved, especially when the interfacial area is middle size (PANI-8) in concentration-up series, the second endothermic transition can be barely found. However, in Fig. 6(C), the DSC curve of PANI-PAMPSA sample has a larger endothermic peak at lower temperature range, which again demonstrates that PANI-PAMPSA can be degraded more easily.

3.5. Electrical conductivity (σ)

Fig. 7 depicts the room-temperature σ of the PANI nanostructures. With polymerization time extended (PANI-1, PANI-2, PANI-3), the σ of the PANI NFs is almost the same. However, the σ is obviously improved when the scale is decreased (PANI-4 vs PANI-2), which is associated with the morphology of the PANI NFs. From Fig. 3 and Table 2, PANI-4 with a higher aspect ratio of 9.53 is observed to have a higher σ than that of PANI-2 with an aspect ratio of 7.01 [70,71]. For interfacial series (PANI-4, PANI-5, and PANI-6), no obvious change of σ is observed. Similarly, the increased concentration (PANI-7 vs PANI-2) has negligible effect on σ, although concentration-up will increase the crystallinity of the PANI NFs, which has a positive effect on the σ. Meanwhile, more aggregation of the PANI NFs is observed in PANI-7 and PANI-8, which is unfavorable for σ [72]. In addition, the aspect ratio of the NFs of PANI-7 (5.59) and PANI-8 (3.83) is much smaller than that of the PANI-2 (7.01).

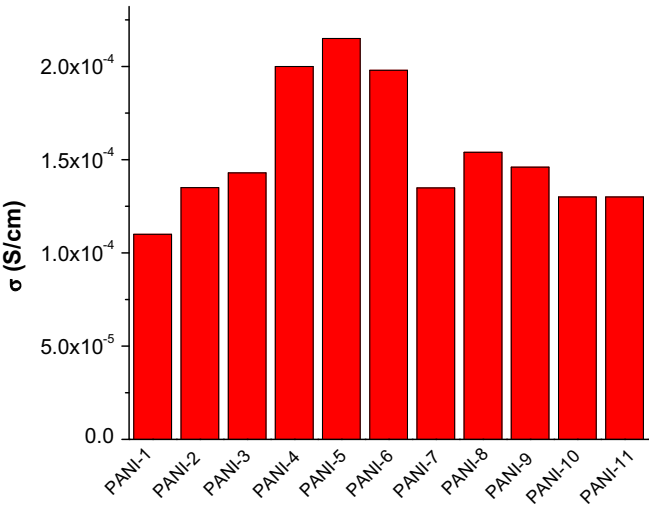

Fig. 7. Electrical conductivity of PANI nanofibers prepared in different conditions and methods, PANI nanoparticles (PANI-10), PANI-PAMPSA (PANI-11).

Compared with the σ of PANI nanostructures prepared with different methods, ultrasonication (PANI-10) and polymer acid doping (PANI-11), PANI NFs (PANI-2) have a slightly higher σ than that of the PANI NSs (PANI-10), which is associated with the poorer crystallinity and lower aspect ratio of nanosphere samples. Although PANI-PAMPSA (PANI-11) has sharp peaks in the XRD pattern, most of which can be tracked from oxidant, and the crystallinity of the peaks belong to PANI is pretty lower (6.93%) than the crystallinity of 9.42% for PANI-2 and 7.48% for PANI-10, which leads a lower σ.

Fig. 8(A) shows the resistivity as a function of temperature for the PANI NFs prepared with different conditions. Both increased concentration (PANI-7 vs PANI-2) and decreased interfacial area (PANI-4, PANI-5, and PANI-6) cause an increased resistivity. And for scale-down sample (PANI-4 vs PANI-2), the resistivity of PANI-4 is higher than that of PANI-2 in the low temperature range. However, with increasing temperature, the resistivity of PANI-4 becomes lower than that of PANI-2. In addition, the resistivity of the PANI NFs is lower than that of the PANI NPs. And PANI-PAMPSA has the highest resistivity compared with those of the PANI NFs and PANI NPs, Fig. 8(B). And the change of resistivity can be associated with the electron transportation mechanism.

The electron transportation mechanism is investigated by exploring the relationship between temperature and σ, using Equation (3) [9,73]:

$$\sigma = \sigma_0 \exp\left[-\left(\frac{T_0}{T}\right)^{1/n}\right] \tag{3}$$

T_0 is the characteristic Mott temperature related to the electronic wave-function localization degree and σ_0 is the conductivity at infinite high temperature, the value of n can equal to 4, 3 and 2 representing three, two and one dimension. Here n is equal to 4, which is the best fit for each sample, Fig. 8 (C&D), indicating a 3-d variable range hopping (VRH) behavior. And it is observed that the PANI NFs (PANI-4) with the highest aspect ratio have the lowest resistivity. For the hopping electron, it will choose a way with the lowest energy consumption and shortest distance, and the energy of electron hopping between the fibers should be higher than the energy hopping along the fibers owing to the contact resistance between fibers. In addition, in a 3-d VRH electron transportation system, the junctions of the PANI NFs with higher aspect ratio are fewer than those in the PANI NFs with lower aspect ratio. Thus, the PANI NFs (PANI-4) with the highest aspect ratio have the lowest conductivity [74].

3.6. Dielectric permittivity

Fig. 9(A&B) shows the real permittivity (ε') and imaginary permittivity (ε'') of the PANI NFs, respectively. Both ε' and ε'' can be divided into three stages. In the lower frequency region (20–110 Hz), ε' increases and ε'' decreases sharply with increasing frequency. During 110-10^5 Hz, the slopes of both curves become small. And in the higher frequency region (10^5–2×10^6 Hz), both ε' and ε'' tend to be constant with increasing frequency.

In the whole frequency range, ε' keeps negative and increases with increasing frequency. On the contrary, ε'' is always positive and decreases with increasing frequency. And thus, the dielectric loss ($\tan\delta$) value of the PANI nanofiber samples, Fig. 9(C), which is the ratio of ε' and ε'', is negative and increases with increasing frequency. And in higher frequency region (10^5–2×10^6 Hz), $\tan\delta$ gets close to zero. And such lower dielectric loss ($\tan\delta$) in high frequency can be useful in supercapacitor field [9]. The negative $\varepsilon'$and high value of σ indicate a disordered motion of the charge carriers along the backbone of the conjugated polymer, and

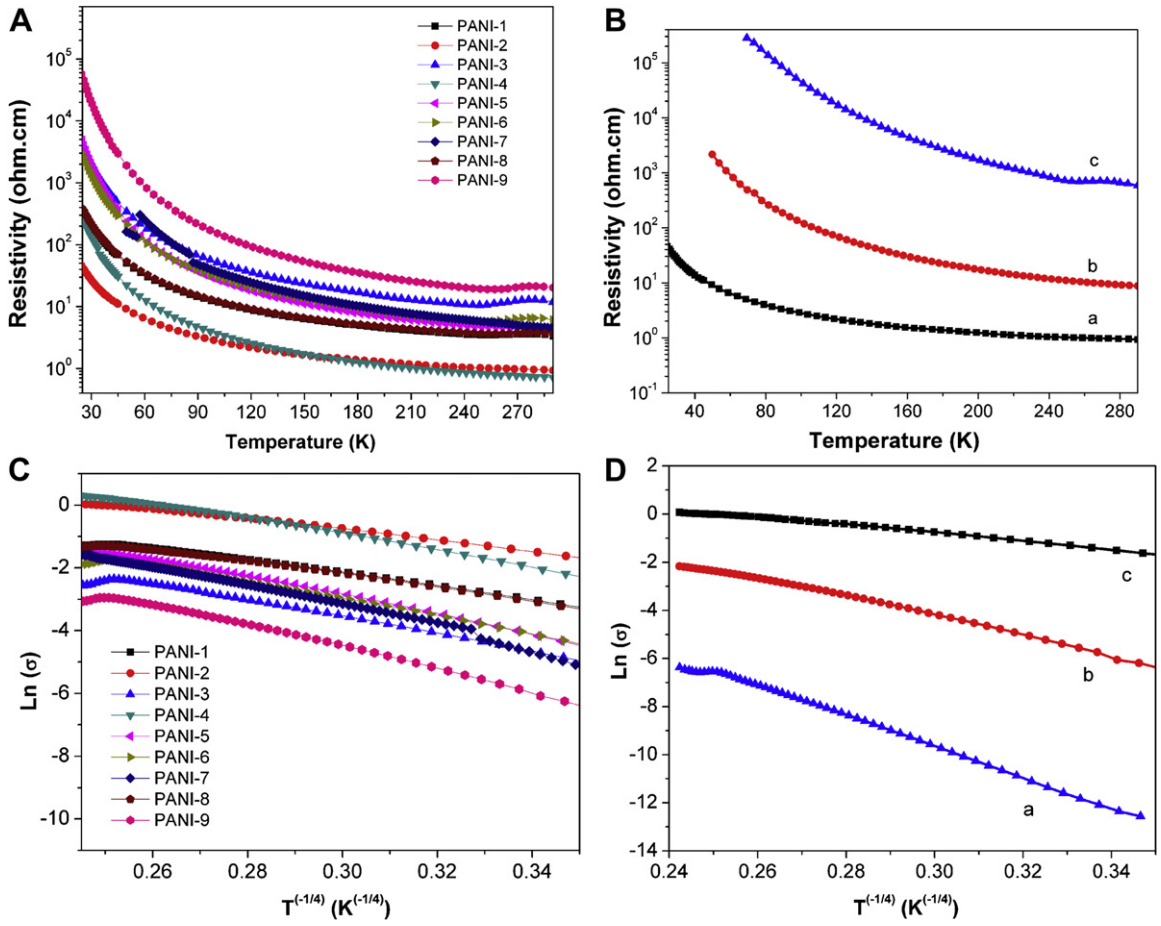

Fig. 8. (A) Resistivity vs temperature of PANI nanofibers prepared in different conditions, (B) Resistivity vs temperature of (a) PANI nanofibers, (b) PANI nanoparticles, (c) PANI-PAMPSA (C) $\ln(\sigma)$ vs $T^{-1/4}$ of PANI nanofibers prepared in different conditions, and (D) $\ln(\sigma)$ vs $T^{-1/4}$ of (a) PANI-PAMPSA, (b) PANI nanoparticles, (c) PANI nanofibers.

which in turn could improve the microwave behavior [75], indicating that these PANI NFs are good candidates for electromagnetic field shielding. The negative real permittivity is also observed in PANI due to the delocalization of charge carrier in a macroscopic scale, which induces the negative permittivity, and is caused by the instinct metallic state in PANI [76,77]. In early study of metallic property of conducting PANI, the data is consistent with the Drude model, in which the relationship between the permittivity and frequency can be written as Equation (4) [61]:

$$\varepsilon'(\omega) = \varepsilon_\infty - \left[\omega_p^2\tau^2\left(1+\omega^2\tau^2\right)^{-1}\right] \tag{4}$$

where ω_p is the screened plasma frequency, ω is the test frequency, τ means free time between ionic collisions, ε_∞ is the high frequency dielectric constant, since ε_∞, τ, ω_p are constant, which can be calculated, with the value of ω increase, the value of $\varepsilon'(\omega)$ should increase. And as expected, at the screen plasma frequency, the values of $\varepsilon'(\omega)$ will cross zero and become negative at all frequencies below certain frequency [61]. What is observed in our test exactly follows the same trend, with the frequency increase, the value of permittivity increases, which completely corresponds to the equation. The lower value of ε' of the sample with short fibers (PANI-5, PANI-7 and PANI-8) is attributed to the tight contact of the NFs compared with the longer ones (PANI-2 and PANI-3) in the presses samples. And tight contact is beneficial for the movement of charge carriers.

For PANI NPs and PANI-PAMPSA samples, Fig. 10(A&B), PANI NPs have a similar change tendency of ε' and ε'' with PANI NFs. In the lower frequency range (20–10^3 Hz), the ε' of PANI NPs is lower than that of the PANI NFs, however, with the frequency increased, the ε' of the PANI NPs is almost the same as that of the PANI NFs. On the contrary, PANI-PAMPSA has positive ε' and negative ε'' in the lower frequency region, and with the increase of the frequency, ε' decreases to negative and ε'' increases to positive. The positive real permittivity of PANI-PAMPSA is consistent with the derived electron transportation mechanism. The obtained T_0 and σ_0 values for each sample from the electron transportation part are summarized in Table 5. It is worth noting that T_0 of PANI-PAMPSA (148.62×10^5 K) hybrid is much higher than that of the PANI NPs (26.40×10^5 K) and PANI NFs (1.39×10^5 K), and larger T_0 indicates stronger localization of charge carriers [9], which causes the difference of permittivity change. The lowest value of dielectric loss ($\tan\delta$) of PANI-PAMPSA appears at 100 Hz, Fig. 10 (C), which is attributed to the much larger increases of ε'' than the lower decrease of ε' in lower frequency range.

3.7. Magnetoresistance properties

The magnetoresistance (MR), $(R(H,T) - R(0,T)/R(H,T))$ is defined as a resistance change when the relative orientation of the magnetic domains in adjacent layers is adjusted from anti-parallel to parallel under an applied magnetic field [50]. Normally, two theories are used to interpret the resistance change in materials

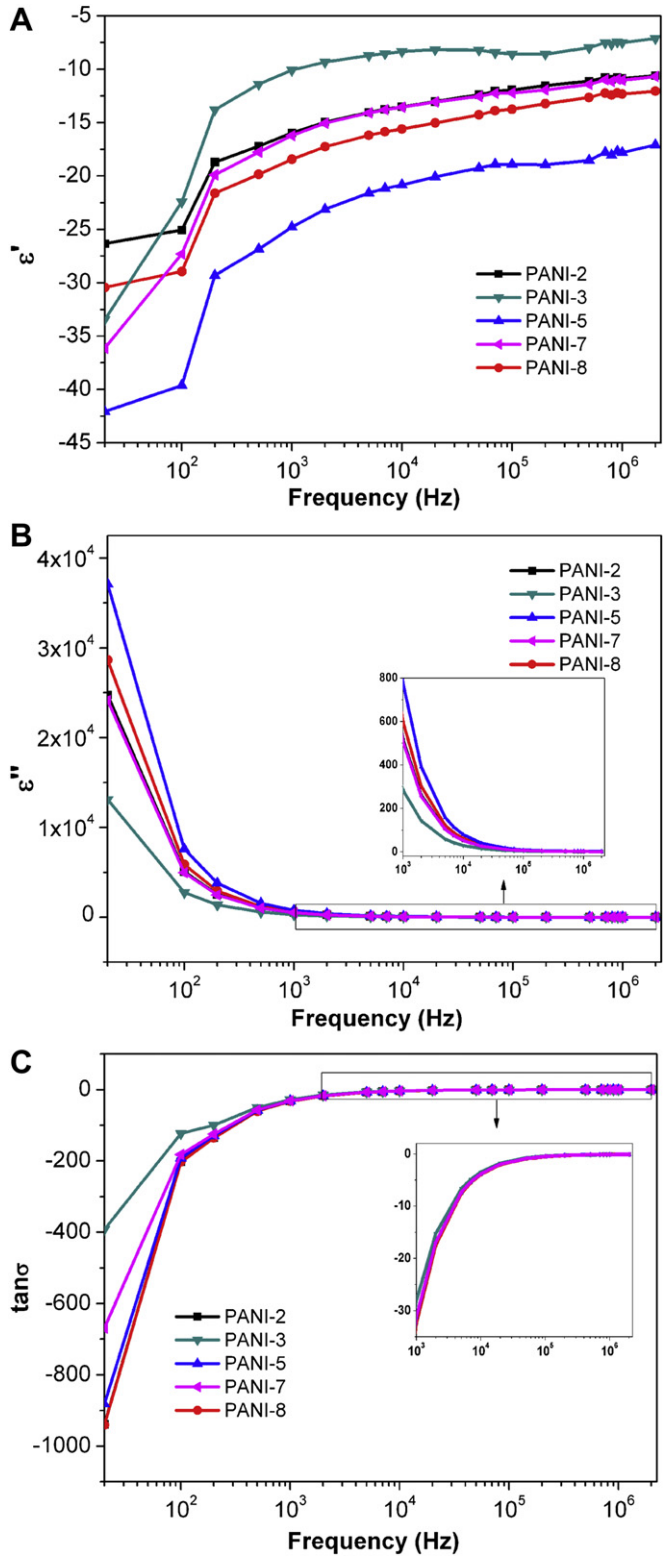

Fig. 9. (A) Real permittivity, (B) Imaginary permittivity, and (C) Dielectric loss of PANI nanofibers prepared in different conditions.

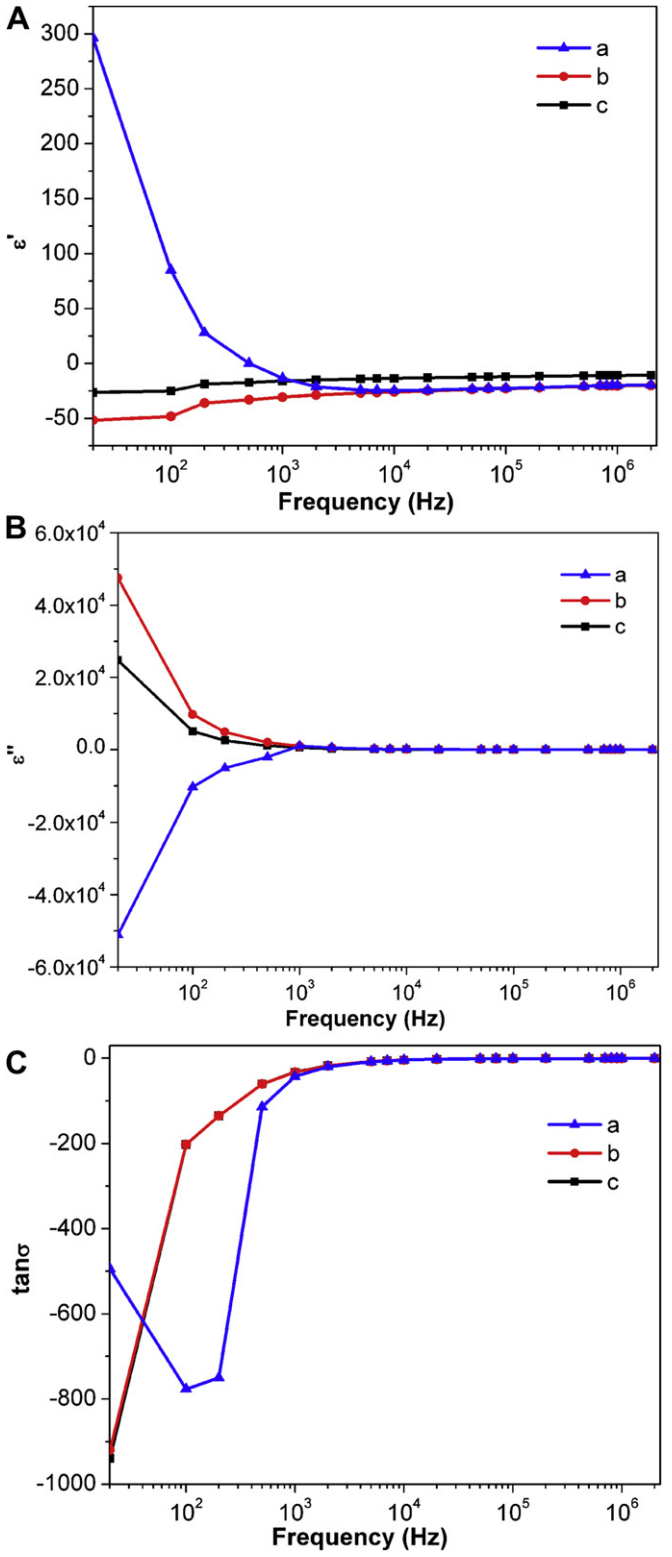

Fig. 10. (A) Real permittivity (ε') of (a) PANI-PAMPSA, (b) PANI nanoparticles, (c) PANI nanofibers; (B) Imaginary permittivity (ε'') of (a) PANI-PAMPSA, (b) PANI nanoparticles, (c) PANI nanofibers; and (C) Dielectric loss ($\tan\delta$) of (a) PANI-PAMPSA, (b) PANI nanoparticles, (c) PANI nanofibers.

under an applied magnetic field. Forward interference model [78,79] is used to explain the negative MR, the effect of interference among various hopping paths between hopping sites is considered and is expressed in Equation (5):

$$\frac{\Delta R(H,T)}{R(0,T)} = \frac{\rho(H,T)-\rho(0,T)}{\rho(0,T)} \approx -C_{\mathrm{sat}}\frac{H}{H_{\mathrm{sat}}} \tag{5}$$

Table 5
T_0 and σ_0 of the PANI nanofibers prepared in different conditions, PANI nanoparticles, and PANI doped with PAMPSA.

Samples	$T_0 \times 10^5$ (K)	σ_0 (S/cm)
PANI-1	3.71	168.54
PANI-2	1.39	141.35
PANI-3	9.77	306.34
PANI-4	9.03	3670.01
PANI-5	18.23	2936.49
PANI-6	11.14	741.53
PANI-7	9.45	460.49
PANI-8	3.91	178.99
PANI-9	26.31	1587.69
PANI nanofiber (PANI-2)	1.39	141.35
PANI nanoparticle	26.40	2480.19
PANI-PAMPSA	148.62	7817.89

C_{sat} is the saturation constant and H_{sat} is the effective saturation magnetic field, the resistance will decrease with the addition of magnetic field. Slightly negative MR is observed in PANI in early study of PANI nanocomposites [80].

On the contrary, the external magnetic field will cause an increase of the resistance, which is associated with the wave-function shrinkage model [79]. In this theory, the magnetic field leads to the contraction of the electronic wave function at impurity center and results in the reduction of the hopping probability between two sites, which in turn cause the positive MR. In this theory, MR is given by Equation (6):

$$\frac{\Delta R(H,T)}{R(0,T)} \approx t_2 \frac{H^2}{H_C^2}\left(\frac{T_{Mott}}{T}\right)^{1/4} \tag{6}$$

Here, $t_2 = (5/2016) \times 36$ is a numerical constant and $H_C = 6\hbar[ea_0^2(T_{Mott}/T)^{1/4}]$, H_C is the normalized intrinsic magnetic field, a_0 is the localization length. The introduction of a magnetic field contracts the localization site and causes the decrease of a_0, which then increases the resistance $R(H,T)$.

The MR of PANI vs $H^{1/3}$ is shown in Fig. 11. Generally, the MR of PANI is proportional to $H^{1/3}$ (H is the magnetic field) at high magnetic fields [81]. All the samples, i.e., PANI NFs (PANI-8 and PANI-9), PANI NPs (PANI-10) and PANI-PAMPSA (PANI-11) exhibit a positive MR and proportional to $H^{1/3}$. In strong magnetic fields [81], Equation (7)

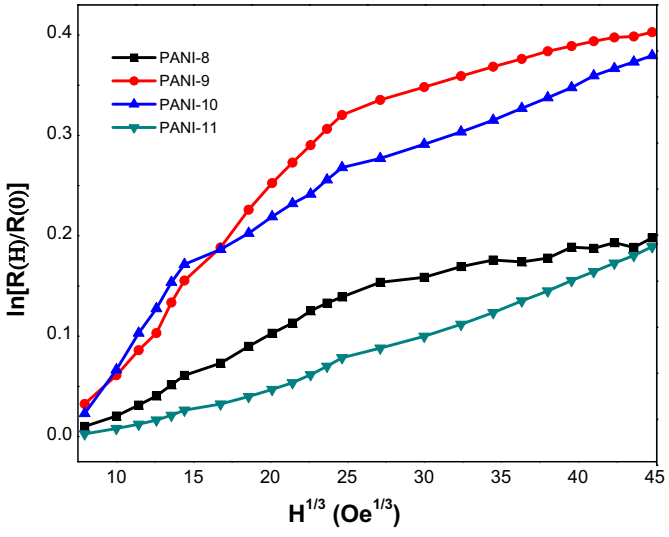

Fig. 11. $\ln[R(H,T)/R(0,T)]$ vs $H^{1/3}$ of PANI nanofibers (PANI-8 and PANI-9), PANI nanoparticles (PANI-10), and PANI-PAMPSA (PANI-11).

$$\ln[\rho(H,T)/\rho(0,T)] = \left(2.1eH/N(E)c\hbar L_H k_B T^3\right)^{1/3} \tag{7}$$

Here, k_B is the Boltzmann constant, $N(E)$ is the density of state at the Fermi level, $\hbar$ is the Planck constant, e is the electronic charge, c is the velocity of light, and L_H is the magnetic length. When H and T are constant, the slope of $\ln[R(H,T)/R(0,T)]$ vs $H^{1/3}$ is only related to $N(E)$, larger MR indicates less $N(E)$, thus PANI-PAMPSA (PANI-11) has higher density of state at the Fermi level in strong magnetic fields than PANI nanoparticles (PANI-10).

4. Conclusion

The influences of the synthesis methods (interfacial polymerization, ultrasonication, and polymer acid doping) on the morphology and physicochemical properties of the polyaniline nanostructures are investigated. Among the PANI nanostructures prepared by the three different methods, only the interfacial polymerization yields nanofiber morphology, nanoparticles are observed from ultrasonication. However, PANI doped with PAMPSA polymer acid possesses unique flake-like structure. The crystalline structure of PANI-PAMPSA with an observed XRD peak shifting to higher degree is different from that of the nanostructures synthesized by the other two methods. In the interfacial polymerization, the effects of the polymerization time, interfacial surface area, and the concentration of the reactants on the microstructures and the physicochemical properties have been studied. The morphology of the PANI NFs can be controlled by varying synthesis conditions. Among all the PANI NFs, the decreased scale (PANI-4 vs PANI-2) provides NFs with larger aspect ratio and the conductivity is higher than other samples. And the increased concentration (PANI-7 vs PANI-2) causes thinner PANI NFs with an improved thermal stability owing to the increased crystallinity. Interfacial area also affects the morphology of the PANI NFs with decreased interfacial area leading to shorter NFs. The NFs with larger length are observed to have lower resistivity due to the 3-d variable range electron hopping conduction mechanism. The PANI NFs have lower resistance than the PANI NPs and PANI-PANPSA. Both kinds of nanostructural PANI (NFs and NPs) have negative permittivity in the whole frequency range, however, PANI-PAMPSA has positive permittivity in the lower frequency range. The dielectric loss of all PANI is negligible in higher frequency range, indicating a less energy loss if serving as supercapacitor. The positive magnetoresistance in all three kinds of PANI is observed and theoretically analyzed by the wave-function shrinkage model.

Acknowledgment

This project is supported by the National Science Foundation-Nanoscale Interdisciplinary Research Team and Materials Processing and Manufacturing (CMMI 10-30755) managed by Dr. Mary Toney. D.P. Young acknowledges support from the NSF under Grant No. DMR 10-05764. S. Wei acknowledges the Welch foundation (V-0004).

References

[1] Smela E. Adv Mater 2003;15:481–94.
[2] Bradley DDC. Synth Met 1993;54:401–15.
[3] Zhu J, Wei S, Alexander Jr M, Cocke D, Ho TC, Guo Z. J Mater Chem 2010;20:568–74.
[4] Zhu J, Wei S, Alexander MJ, Dang TD, Ho TC, Guo Z. Adv Funct Mater 2010;20:3076–84.
[5] Ding K, Jia H, Wei S, Guo Z. Ind Eng Chem Res 2011;50:7077–82.
[6] Rudge A, Raistrick I, Gottesfeld S, Ferraris JP. Electrochim Acta 1994;39:273–87.
[7] Mavinakuli P, Wei S, Wang Q, Karki AB, Dhage S, Wang Z, et al. J Phys Chem C 2010;114:3874–82.

[8] Zhu J, Wei S, Zhang L, Mao Y, Ryu J, Mavinakuli P, et al. J Phys Chem C 2010; 114:16335–42.
[9] Zhu J, Wei S, Zhang L, Mao Y, Ryu J, Karki AB, et al. J Mater Chem 2011;21: 342–8.
[10] Zhu J, Wei S, Zhang L, Mao Y, Ryu J, Haldolaarachige N, et al. J Mater Chem 2011;21:3952–9.
[11] Wei S, Mavinakuli P, Wang Q, Chen D, Asapu R, Mao Y, et al. J Electrochem Soc 2011;158(11):K205–12.
[12] Moon HS, Park JK. Synth Met 1998;92:223–8.
[13] Tarver J, Yoo JE, Dennes TJ, Schwartz J, Loo YL. Chem Mater 2009;21: 280–6.
[14] Yoo JE, Cross JL, Bucholz TL, Lee KS, Espe MP, Loo YL. J Mater Chem 2007;17: 1268–75.
[15] Yang X, Li B, Wang H, Hou B. Prog Org Coat 2010;69:267–71.
[16] Dhawan SK, Kumar D, Ram MK, Chandra S, Trivedi DC. Sens Actuators B 1997; 40:99–103.
[17] Olad A, Nabavi R. J Hazard Mater 2007;147:845–51.
[18] Li M, Guo Y, Wei Y, MacDiarmid AG, Lelkes PI. Biomaterials 2006;27: 2705–15.
[19] Yang SM, Chen JT. Synth Met 1995;69:153–4.
[20] Gorman CB, Biebuyck HA, Whitesides GM. Chem Mater 1995;7:526–9.
[21] Jing X, Wang Y, Wu D, Qiang J. Ultrason Sonochem 2007;14:75–80.
[22] Yue J, Epstein AJ. J Am Chem Soc 1990;112:2800–1.
[23] Chen SA, Hwang GW. J Am Chem Soc 1994;116:7939–40.
[24] Lin HK, Chen SA. Macromolecules 2000;33:8117–8.
[25] McCarthy PA, Huang J, Yang SC, Wang HL. Langmuir 2002;18:259–63.
[26] Roy S, Fortier JM, Nagarajan R, Tripathy S, Kumar J, Samuelson LA, et al. Biomacromolecules 2002;3:937–41.
[27] Wei X, Epstein AJ. Synth Met 1995;74:123–5.
[28] Innis PC, Norris ID, KaneMaguire LAP, Wallace GG. Macromolecules 1998;31: 6521–8.
[29] Kwang SL, Graciela BB, Feng G, Yueh LL. AIP 2005;86:074102–4.
[30] Virji S, Huang J, Kaner RB, Weiller BH. Nano Lett 2004;4:491–6.
[31] Fan Z, Wang Z, Duan M, Wang J, Wang S. J Membr Sci 2008;310:402–8.
[32] Sadek AZ, Wlodarski W, Shin K, Kaner RB, Kalantar-zadeh K. Synth Met 2008; 158:29–32.
[33] Hung CC, Wen TC, Wei Y. Mater Chem Phys 2010;122:392–6.
[34] Jang J, Bae J, Lee K. Polymer 2005;46:3677–84.
[35] Banerjee S, Kumar A. J Phys Chem Solids 2010;71:381–8.
[36] Deka M, Nath AK, Kumar A. J Membr Sci 2009;327:188–94.
[37] Kim HS, Hobbs HL, Wang L, Rutten MJ, Wamser CC. Synth Met 2009;159: 1313–8.
[38] Li J, Fang K, Qiu H, Li S, Mao W, Wu Q. Synth Met 2004;14:191–4.
[39] Qiu H, Qi S, Wang D, Wang J, Wu X. Synth Met 2010;160:1179–83.
[40] Yang N, Zhai J, Wan M, Wang D, Jiang L. Synth Met 2010;160:1617–22.
[41] Choi SS, Young Chu B, Sun Hwang D, Goo Lee S, Ho Park W, Kyoo Park J. Thin Solid Films 2005;477:233–9.
[42] Li X, Tian S, Ping Y, Kim DH, Knoll W. Langmuir 2005;21:9393–7.
[43] Pinto NJ, Ramos I, Rojas R, Wang PC, Johnson Jr AT. Sens Actuators B 2008;129: 621–7.
[44] Aussawasathien D, Dong JH, Dai L. Synth Met 2005;154:37–40.
[45] Zussman E, Yarin AL, Bazilevsky AV, Avrahami R, Feldman M. Adv Mater 2006; 18:348–53.
[46] Yu JH, Fridrikh SV, Rutledge GC. Adv Mater 2004;16:1562–6.
[47] Feng C, Khulbe KC, Matsuura T. J Appl Polym Sci 2010;115:756–76.
[48] Huang J, Kaner RB. J Am Chem Soc 2003;126:851–5.
[49] Huang J, Virji S, Weiller BH, Kaner RB. J Am Chem Soc 2002;125:314–5.
[50] Baibich MN, Broto JM, Fert A, Van Dau FN, Petroff F, Etienne P, et al. Phys Rev Lett 1988;61:2472–5.
[51] Bobbert PA, Wagemans W, van Oost FWA, Koopmans B, Wohlgenannt M. Phys Rev Lett 2009;102:156604.
[52] Prigodin VN, Bergeson JD, Lincoln DM, Epstein AJ. Synth Met 2006;156: 757–61.
[53] Bloom FL, Wagemans W, Kemerink M, Koopmans B. Phys Rev Lett 2007;99: 257201.
[54] Wagemans W, Schellekens AJ, Kemper M, Bloom FL, Bobbert PA, Koopmans B. Phys Rev Lett 2011;106:196802.
[55] Xiong ZH, Wu D, Valy Vardeny Z, Shi J. Nature 2004;427:821–4.
[56] Zhu J, Wei S, Ryu J, Guo Z. J Phys Chem C 2011;115:13215–22.
[57] Hoffman AJ, Alekseyev L, Howard SS, Franz KJ, Wasserman D, Podolskiy VA, et al. Nat Mater 2007;6:946–50.
[58] Pendry JB, Holden AJ, Stewart WJ, Youngs I. Phys Rev Lett 1996;76:4773–6.
[59] Dolgov OV, Kirzhnits DA, Maksimov EG. Rev Mod Phys 1981;53:81–93.
[60] Jin CY, Zhu BS, Wang XF, Lu QH. Chem Res Toxicol 2008;21:1871–7.
[61] Lee K, Cho S, Heum Park S, Heeger AJ, Lee CW, Lee SH. Nature 2006;441:65–8.
[62] Pouget JP, Jozefowicz ME, Epstein AJ, Tang X, MacDiarmid AG. Macromolecules 1991;24:779–89.
[63] Moon HS, Park JK. J Polym Sci Part A Polym Chem 1998;36:1431–9.
[64] Clauss J, Schmidt-Rohr K, Adam A, Boeffel C, Spiess HW. Macromolecules 1995;25:5208–14.
[65] Tsutsumi H, Fukuzawa S, Ishikawa M, Morita M, Matsuda Y. Synth Met 1995; 72:231–5.
[66] Ahmed SM. Eur Polym J 2002;38:1151–8.
[67] Palaniappan S, Narayana BH. Thermochim Acta 1994;237:91–7.
[68] Lu X, Ng HY, Xu J, He C. Synth Met 2002;128:167–78.
[69] Chen T, Dong C, Li X, Gao J. Polym Degrad Stab 2009;94:1788–94.
[70] Agari Y, Ueda A, Nagai S. J Appl Polym Sci 1991;43:1117–24.
[71] Yu QZ, Shi MM, Deng M, Wang M, Chen HZ. Mater Sci Eng B 2008;150:70–6.
[72] Xing S, Zhao C, Jing S, Wang Z. Polymer 2006;47:2305–13.
[73] Guo Z, Shin K, Karki A, Young D, Kaner R, Hahn H. J Nanopart Res 2009;11: 1441–52.
[74] Yu D, Wang C, Wehrenberg BL, Guyot-Sionnest P. Phys Rev Lett 2004;92: 216802.
[75] Phang SW, Hino T, Abdullah MH, Kuramoto N. Mater Chem Phys 2007;104: 327–35.
[76] Liu CD, Lee SN, Ho CH, Han JL, Hsieh KH. J Phys Chem C 2008;112:15956–60.
[77] Joo J, Oh EJ, Min G, MacDiarmid AG, Epstein AJ. Synth Met 1995;69:251–4.
[78] Jaiswal M, Wang W, Fernando KAS, Sun YP, Menon R. Phys Rev B 2007;76: 113401.
[79] Su TI, Wang CR, Lin ST, Rosenbaum R. Phys Rev B 2002;66:054438.
[80] Long Y, Chen Z, Duvail JL, Zhang Z, Wan M. Physica B. 2005;370:121–30.
[81] Aleshin AN, Lee K, Lee JY, Kim DY, Kim CY. Synth Met 1999;99:27–33.